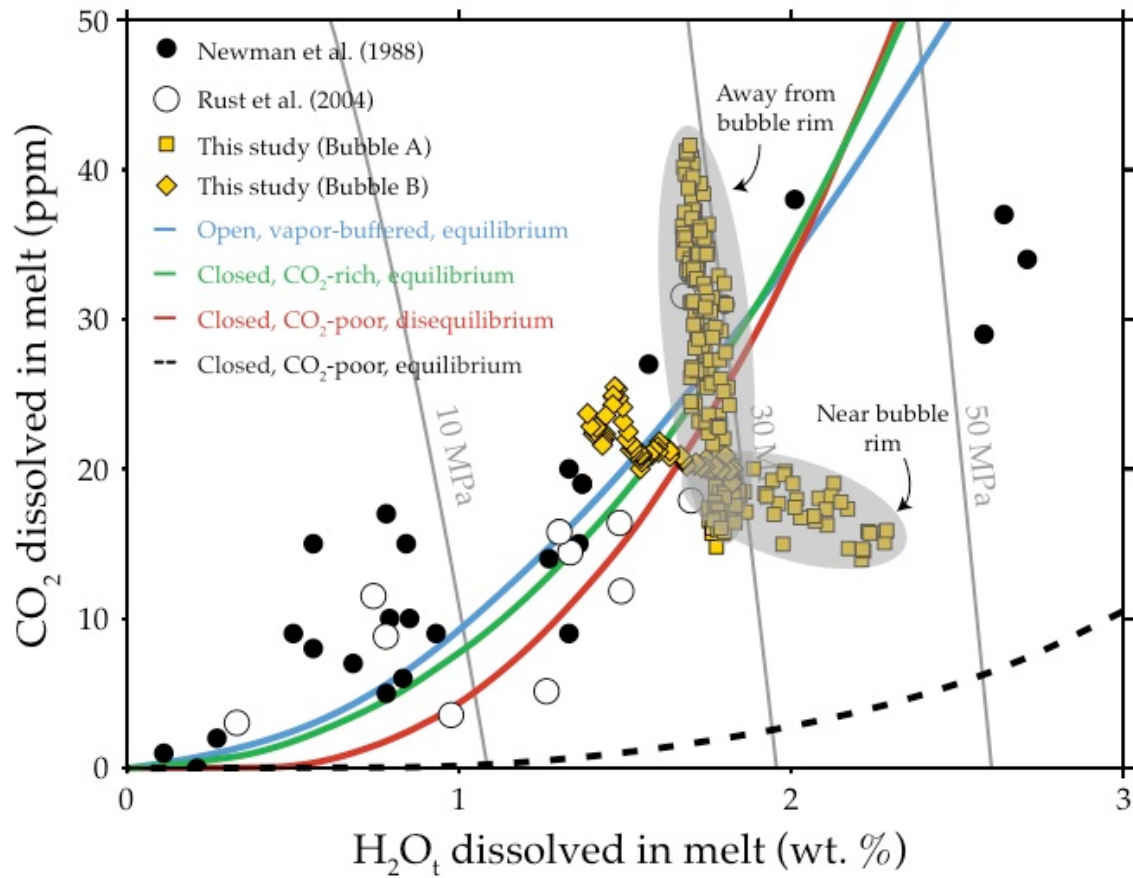


1

## Supplemental information

### I. Alternative version of figure 1



3

4 **Figure A1.**  $\text{CO}_2$  versus  $\text{H}_2\text{O}$  for Mono Craters pyroclasts. Circles represent spot analyses on  
 5 obsidian clasts. Squares and diamonds represent data from transects within individual clasts.

### II. Sample preparation

7 Three obsidian clasts from beds 2 and 7 were selected for analysis. Doubly-polished thin  
 8 sections (approximately 100-300  $\mu\text{m}$  thick) were prepared following methods described  
 9 in Watkins et al. (2008). Each wafer has at least one bubble with radius much greater than  
 10 the wafer thickness so that effects of bubble curvature on volatile concentration  
 11 measurements can be neglected. In addition to samples bearing at least one bubble, we  
 12 determined that the glass should contain greater than about 20 ppm dissolved  $\text{CO}_2$  to be

13 above detection limits for relatively thin (ca. 200  $\mu\text{m}$ ) wafers. Our sample selections were  
14 fortuitous in this respect since it is impossible to tell by visual inspection whether an  
15 individual clast will be volatile-rich.

16

17 **III. SS-FTIR measurements**

18 Concentrations of total water ( $\text{H}_2\text{O}_t$ ) and  $\text{CO}_2$  were determined by synchrotron radiation-  
19 source Fourier Transform Infrared Spectroscopy (SR-FTIR) at the Advanced Light  
20 Source beamline 1.4.3 using a Nicolet Magna 760 FTIR Spectrometer interfaced with a  
21 Nic-Plan IR microscope. Measurements were made using a 32x Reflachromat objective,  
22 MCT A detector and KBr beamsplitter. The spot size for the infrared beam is diffraction  
23 limited, about 2-4  $\mu\text{m}$  in this spectral region, and the step size between individual  
24 measurements can be as low as 0.1  $\mu\text{m}$ . Transects were oriented perpendicular to bubble  
25 rims and we collected 32 scans per spot and 128 scans for the background. A new  
26 background was collected every 5 minutes during each transect. Since  $\text{CO}_2$  was found to  
27 be near detection limits, we performed several tests to ensure that contamination from the  
28 atmosphere was minimal, including repeated measurements on different days. From the  
29 baseline fitting used in FTIR spectroscopy, we estimate the relative uncertainty between  
30 adjacent points to be <10% for  $\text{CO}_2$ , and <2% for water species (OH and  $\text{H}_2\text{O}_m$ ). Figure  
31 A2 shows a picture of a typical background-subtracted absorbance spectrum for a  
32 relatively volatile-rich rhyolite glass.

33

34 Concentrations were determined using the Beer-Lambert law:

35

$$C_i = \frac{M_i A}{\rho d \epsilon_i}$$

36

37

38 where  $M_i$  is the molecular weight (g/mol),  $A$  is the absorbance (height or area),  $\rho$  is the  
39 sample density ( $\approx 2300$  g/L for rhyolite glass),  $d$  is the thickness of the wafer (cm), and  $\epsilon_i$   
40 is the molar absorption coefficient (L cm/mol). We used molar absorption coefficients for  
41 OH and  $H_2O_m$  from Zhang et al. (1997) and  $CO_2$  from Behrens et al. (2004). The  
42 thickness of the wafer along each transect was measured using the method of Nichols and  
43 Wysoczanski (2007), which allows us to correct for non-uniform sample thickness using  
44 the wavelength of interference fringes in reflectance mode. We used an index of  
45 refraction for rhyolite glass of 1.49 (Tatlock et al., 1976).

46

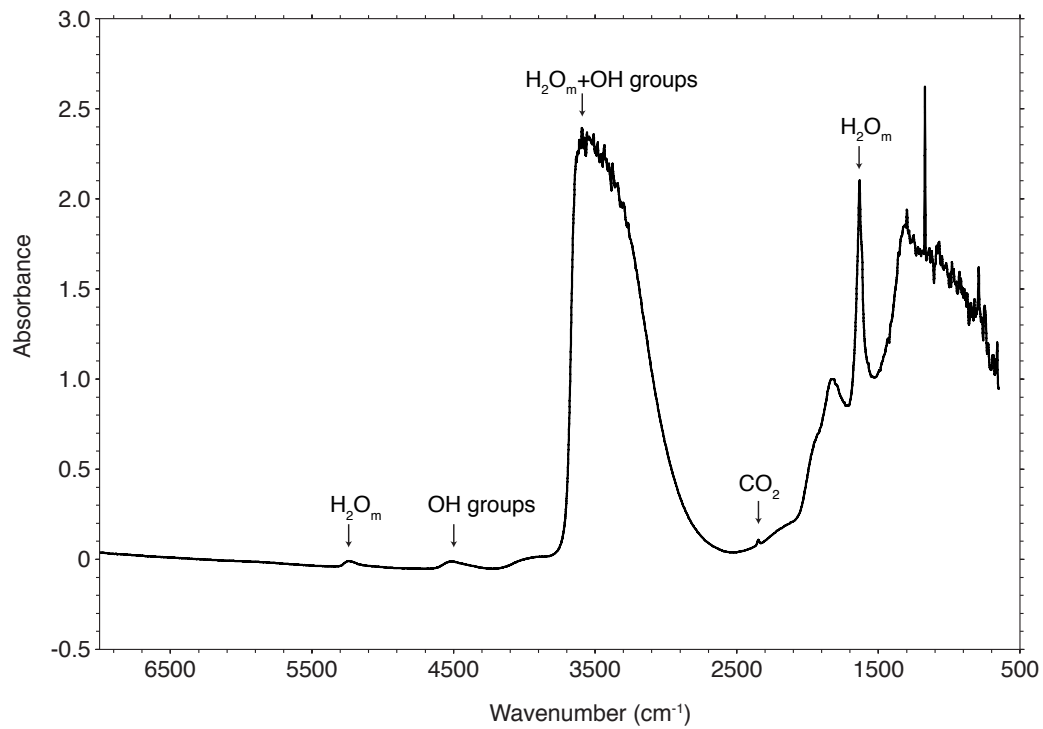


**Figure A2.** FTIR spectrum from a single spot on a doubly-polished obsidian clast from bed 2.

The absorbances at 2350, 4520 and 5230  $\text{cm}^{-1}$  were used to determine concentrations of  $\text{CO}_2$ ,  $\text{OH}$ , and  $\text{H}_2\text{O}_m$ , respectively.

#### IV. Additional transects

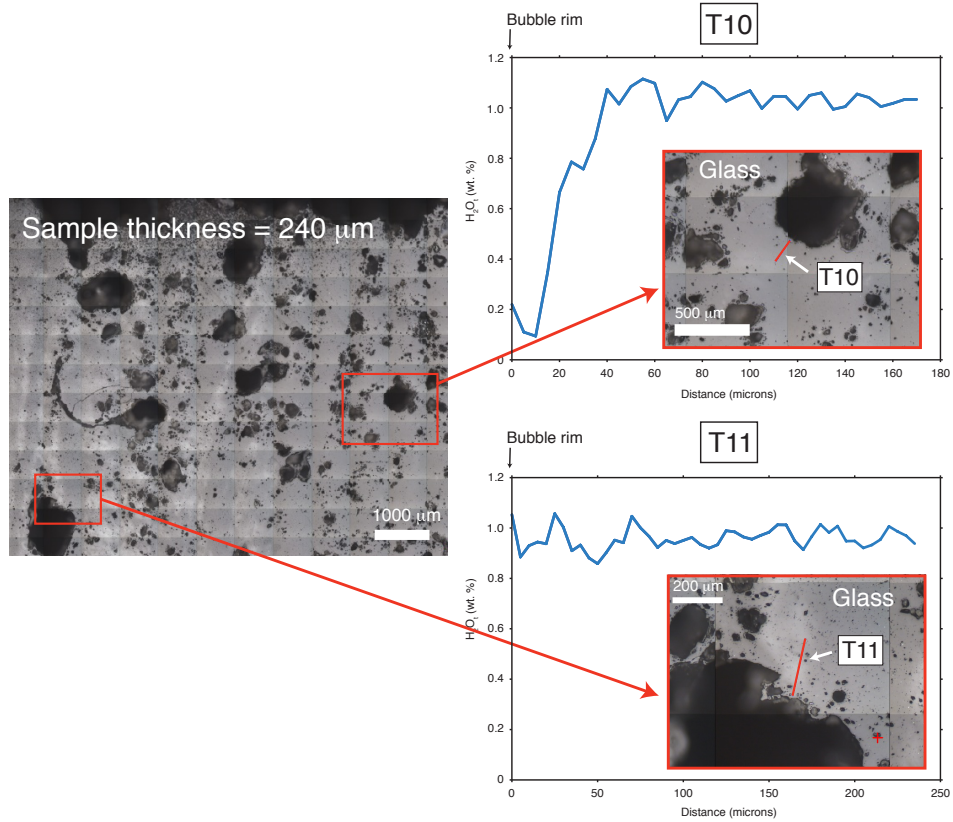


**Figure A3.**  $\text{H}_2\text{O}$  concentration profiles near two bubbles from a bubble-rich obsidian clast. Different clasts, and bubbles within clasts, record different  $P$ - $T$ - $X$  histories in the conduit. Within a single clast, some bubbles appear to be in chemical equilibrium with the melt (T11) while others are surrounded by a melt shell that is depleted in water, characteristic of disequilibrium bubble growth (T10). In these samples,  $\text{CO}_2$  is below detection limits.

47 **V. Mechanisms for bubble resorption**

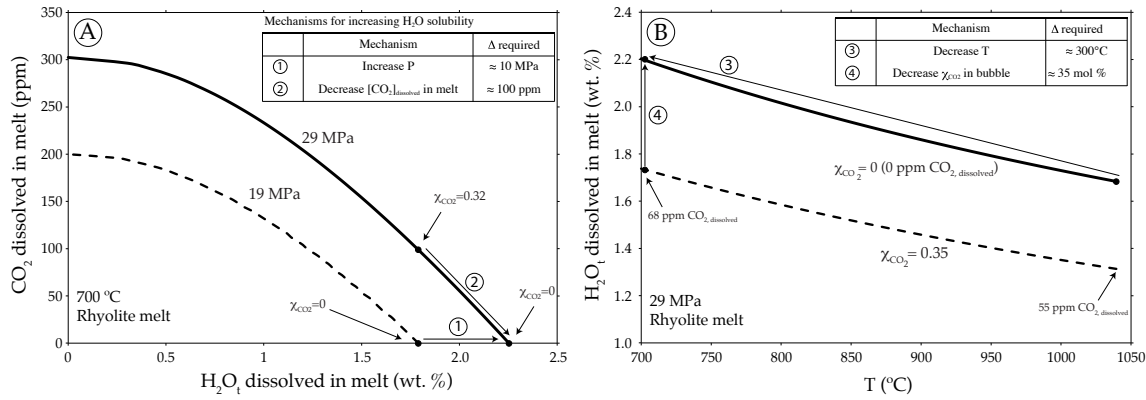
48 Table A1 summarizes the possible mechanisms for resorbing bubbles in the conduit.  
 49 Figures A3 and A4 show how we estimate the magnitude of physical and/or chemical  
 50 changes in the conduit necessary to increase the solubility of water in rhyolite melt from  
 51 about 1.7 to 2.2 wt. %.

## Mechanisms for increasing H<sub>2</sub>O solubility

	Mechanism	Δ required
1	Increase P	≈ 10 MPa
2	Decrease [CO <sub>2</sub> ] <sub>dissolved</sub> in melt	≈ 100 ppm
3	Decrease T	≈ 300°C
4	Vapor fluxing	-

**Table A1.** Mechanisms for resorbing bubbles. For 1, 2, and 3 the magnitudes correspond to an increase in H<sub>2</sub>O solubility from about 1.7 to 2.2 wt. %. Vapor fluxing, on the other hand, causes a reduction in H<sub>2</sub>O solubility; bubbles resorb as water is lost from the melt to fluid-filled fractures.

52



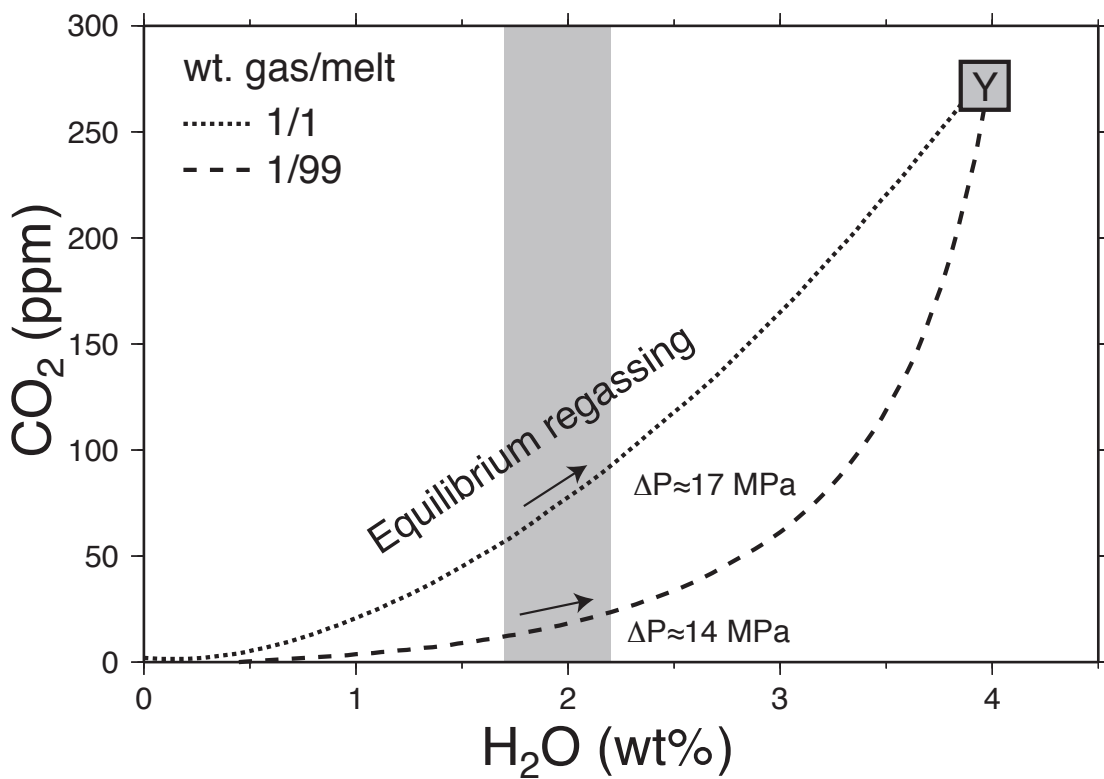
53

54 **Figure A4.** Mechanisms for increasing H<sub>2</sub>O solubility. (a) Equilibrium concentrations of CO<sub>2</sub> and H<sub>2</sub>O dissolved in silicic melt at 700°C (Newman and Lowenstern, 2002). Each line is an isobar and each point on an isobar corresponds to a specific vapor phase composition. At any pressure, a decrease in the CO<sub>2</sub> content of the melt (or vapor) phase results in a decrease in CO<sub>2</sub> solubility and increase in H<sub>2</sub>O solubility. At the same time, the solubilities of both CO<sub>2</sub> and H<sub>2</sub>O increase with increasing pressure. (b) Equilibrium concentration of H<sub>2</sub>O dissolved in silicic melt at 29 MPa (Liu et al., 2005). At any temperature, a decrease in the CO<sub>2</sub> content of the melt (or vapor)

61 phase results in a decrease in  $\text{CO}_2$  solubility and increase in  $\text{H}_2\text{O}$  solubility. At the same time, the  
62 solubilities of both  $\text{CO}_2$  and  $\text{H}_2\text{O}$  increase with decreasing temperature.

63

64 In panel A of figure A4, the  $\Delta P$  is a minimum estimate because we assume there is no  
65  $\text{CO}_2$  in the system. In figure A5 we consider the effect of a pressure increase when  $\text{CO}_2$  is  
66 present. The figure is modified from Rust et al. (2004) and illustrates the importance of  
67 the gas/melt mass ratio on the content of dissolved volatiles in the melt phase. For low  
68 gas/melt ratios, consistent with the formation of obsidian, a pressure increase of about 14  
69 MPa is needed to change the water content of the melt from 1.7 to 2.2 wt. %.  
70 Interestingly, in this scenario the increase in the  $\text{CO}_2$  content of the melt is relatively  
71 minor.



72

73 **Figure A5.** Equilibrium degassing and regassing of a vapor-saturated parent melt (composition  
74 Y) in a closed system (modified from Rust et al., 2004). Curves show degassing trajectories for  
75 two cases that differ in the amount of vapor initially. Dashed curve: During decompression-driven  
76 degassing, the melt has 2.2 wt. % H<sub>2</sub>O at P ≈ 37 MPa and 1.7 wt. % H<sub>2</sub>O P ≈ 23 MPa.

77

78 **VI. Model for bubble resorption**

79 We model the isothermal resorption of a spherical bubble caused by an instantaneous  
80 change in pressure and concomitant increase in water solubility.

81

82 There are three timescales of importance for bubble growth (Gonnermann and Manga,  
83 2007): (1) the timescale for solubility changes due to pressure changes ( $\tau_{dec}$ ), (2) the  
84 timescale for viscous relaxation of the melt around a bubble ( $\tau_\eta = \eta / \Delta P$ ), and (3) the  
85 timescale for volatile diffusion into a bubble ( $\tau_d = R^2 / D$ ). In our problem, we assume the  
86 bubble begins to dissolve after it is compressed, which is valid since the timescale for  
87 viscous relaxation relative to diffusion is effectively instantaneous:

88

89

$$Pe = \frac{\tau_d}{\tau_\eta} = \frac{\Delta P R^2}{\eta D} \approx \frac{(10^7 \text{ Pa}) (10^{-3} \text{ m})^2}{(10^8 \text{ Pa s}) (10^{-12} \text{ m}^2 \text{ s}^{-1})} = 10^5$$

90

91 The viscosity of 10<sup>8</sup> Pa s corresponds to Mono Craters rhyolite (Newman et al., 1988)  
92 with 1.7 wt.% H<sub>2</sub>O<sub>t</sub> at 700°C and was calculated using the model of Hui and Zhang  
93 (2007). For simplicity, and since we do not know the initial or final vapor composition,  
94 we neglect CO<sub>2</sub> altogether and assume the bubble is made entirely of water vapor.

95

96 We begin with a bubble that has grown under equilibrium conditions with respect to H<sub>2</sub>O  
97 so that the concentration of H<sub>2</sub>O in the melt is initially homogeneous. The pressure  
98 increases, the bubble is compressed to a radius of 1 mm, and H<sub>2</sub>O diffuses into the melt.  
99 The concentration of H<sub>2</sub>O in the melt shell evolves according to the one-dimensional  
100 advection-diffusion equation in spherical coordinates:

101

102

$$\frac{\partial c_i}{\partial t} + u_r \frac{\partial c_i}{\partial r} = \frac{1}{r^2} \frac{\partial}{\partial r} \left( D_i r^2 \frac{\partial C_i}{\partial r} \right)$$

103 where  $c_i$  is concentration (moles/m<sup>3</sup>) of component  $i$  ( $i=H_2O_t$  in this case),  $u_r$  (equal to  
104  $dR/dt$  where  $R$  is the radius of the bubble) is the velocity of vapor-melt interface, and  $D_i$   
105 is the diffusivity of H<sub>2</sub>O<sub>t</sub> given by (Zhang et al., 2007):

106

107

$$D_{H_2O_t} = 10^{-12} X \exp(m) \left\{ 1 + \exp \left[ 56 + m + X \left( -34.1 + \frac{44620}{T} + \frac{57.3P}{T} \right) - \sqrt{X} \left( 0.091 + \frac{4.77 \times 10^6}{T^2} \right) \right] \right\}.$$

108

109 Units of  $D_i$  are m<sup>2</sup> s<sup>-1</sup>,  $m = -20.79 - 5030/T - 1.4P/T$ ,  $P$  is in MPa,  $T$  is in Kelvin, and  $X$  is  
110 the mole fraction of water on a single-oxygen basis (Stolper, 1982; Zhang, 2008). As a  
111 further simplification, we approximate the diffusivity of H<sub>2</sub>O<sub>t</sub> as being constant (i.e.,  $X$   
112 corresponds to 1.7 wt. % H<sub>2</sub>O<sub>t</sub>). The boundary conditions for this problem are:

113

114

$$\left( \frac{\partial c_i}{\partial r} \right)_{r=\infty} = 0$$

115 and

116

117  $c_i(r = R) = \text{constant}$

,

118 where *constant* refers to the temperature- and pressure-dependent solubility of  $\text{H}_2\text{O}_i$ ,  
119 which we calculate using the formulation of Liu et al. (2005). At each timestep, the  
120 change in bubble mass is calculated from the flux at the bubble-melt interface using  
121 Fick's first law:

122

123 
$$dn_i = 4\pi R^2 \left( D_i \frac{\partial c_i}{\partial r} \right)_{r=R} dt$$

124 where  $n_i$  refers to the moles of water in the bubble. The radius of the bubble is updated  
125 assuming ideal gas behavior inside the bubble, which is appropriate for bubbles at  
126 shallow depths (Newman et al., 1988).

127

128 We choose  $T=700^\circ\text{C}$ , within the range for the glass transition temperature ( $T_g$ ) of  
129 anhydrous rhyolite (Wright et al., 2007). For comparison, Newman et al. (1988) chose to  
130 model the Mono Craters dataset using  $850^\circ\text{C}$ , Rust et al. (2004) chose  $800^\circ\text{C}$ , and  
131 Gonnermann and Manga (2005) chose  $850^\circ\text{C}$ . The time scales we calculate decrease by  
132 about a factor of 4 in going from  $700^\circ\text{C}$  to  $850^\circ\text{C}$ .

133

134 **Appendix references not cited elsewhere**

135 Behrens, H., Tamic, N., and Holtz, F., 2004, Determination of the molar absorption  
136 coefficient for the infrared absorption band of  $\text{CO}_2$  in rhyolitic glasses, American  
137 Mineralogist, v. 89, p. 301-306.

- 138 Gonnerman, H., and Manga, M., 2007, The fluid mechanics inside a volcano, Annual  
139       Reviews of Fluid Mechanics, v. 39, p. 321-356.
- 140 Hui, H., and Zhang, Y., 2007, Toward a general viscosity equation for natural anhydrous  
141       and hydrous silicate melts, *Geochimica et Cosmochimica Acta*, v. 71, p. 403-416.
- 142 Nichols A., and Wysoczanski, R., 2007, Using micro-FTIR spectroscopy to measure  
143       volatile contents in small and unexposed inclusions hosted in olivine crystals,  
144       *Chemical Geology*, v. 242, p. 371-384.
- 145 Stolper, E., 1982, Water in silicate glasses: An infrared spectroscopic study,  
146       *Contributions to Mineralogy and Petrology*, v. 81, p. 1-17.
- 147 Tatlock, D., Flanagan, F., Bastron, H., Berman, S., and Sutton Jr., A., 1976, Rhyolite,  
148       RGM-1, from Glass Mountain, California, Descriptions and analyses of eight new  
149       USGS rock standards, U.S. Geol. Surv., Prof. Pap., v. 840, p. 11-14.
- 150 Watkins, J., Manga, M., Huber, C., and Martin, M., 2008, Diffusion-controlled spherulite  
151       growth in obsidian inferred from H<sub>2</sub>O concentration profiles, *Contributions to*  
152       *Mineralogy and Petrology*, DOI 10.1007/s00410-0080-327-8.
- 153 Wright, H., Cashman, K., Rosi, M., and Cioni, R., 2007, Breadcrust bombs as indicators  
154       of Vulcanian eruption dynamics at Guagua Pichincha volcano, Ecuador, *Bulletin of*  
155       *Volcanology*, v. 69, p. 281-300.
- 156 Zhang, Y., Belcher, R., Ihinger, P., Wang, L., Xu, Z., and Newman, S., 1997, New  
157       calibration of infrared measurement of dissolved water in rhyolitic glasses,  
158       *Geochimica et Cosmochimica Acta*, v., 61, p. 3089-3100.
- 159 Zhang, Y., 2008, *Geochemical Kinetics*, Princeton University Press, New Jersey, 623 p.
- 160